photonics

MDPI

Review

Design and Characteristics of Photonic Crystal Resonators for Surface-Emitting Quantum Cascade Lasers

Kazuaki Sakoda [1,*], Yuanzhao Yao [1,†], Naoki Ikeda [2], Yoshimasa Sugimoto [2], Takaaki Mano [1], Takashi Kuroda [1], Hirotaka Tanimura [3], Shigeyuki Takagi [3], Rei Hashimoto [4], Kei Kaneko [4], Tsutomu Kakuno [4], Shinji Ohkuma [4], Ryuichi Togawa [4], Tetsuya Miyagawa [4], Hiroshi Ohno [4] and Shinji Saito [4]

[1] Research Center for Functional Materials, National Institute for Materials Science, Tsukuba 305-0044, Japan
[2] Research Network and Facility Service Division, National Institute for Materials Science, Tsukuba 305-0047, Japan
[3] School of Engineering, Tokyo University of Technology, Hachioji 192-0982, Japan
[4] Corporate Manufacturing Engineering Center, Toshiba Corporation, Yokohama 235-0017, Japan
* Correspondence: sakoda.kazuaki@nims.go.jp
† Current address: Department of Applied Physics, University of Tsukuba, Tsukuba 305-8573, Japan.

Abstract: We present our recent development of the surface-emitting quantum cascade laser with a PC (photonic crystal) resonator and a strain-compensated MQW (multiple quantum well) active layer operating at around 4.3 μm. We describe the laser performance mainly from the viewpoint of the design and analysis of the PC resonators, which include both numerical calculations by FEM (finite element method) and analytical calculations using the **k**·**p** perturbation theory and group theory. We analyze the resonance quality factor, overlap factor, extraction efficiency, and far-field pattern, and show how the output power and beam quality have been improved by the appropriate design of the PC resonator.

Keywords: quantum cascade laser; photonic crystal resonator; quality factor; extraction efficiency; finite element method; **k**·**p** perturbation

Citation: Sakoda, K.; Yao, Y.; Ikeda, N.; Sugimoto, Y.; Mano, T.; Kuroda, T.; Tanimura, H.; Takagi, S.; Hashimoto, R.; Kaneko, K.; et al. Design and Characteristics of Photonic Crystal Resonators for Surface-Emitting Quantum Cascade Lasers. *Photonics* **2024**, *11*, 1024. https://doi.org/10.3390/photonics11111024

Received: 17 September 2024
Revised: 17 October 2024
Accepted: 24 October 2024
Published: 30 October 2024

1. Introduction

Quantum cascade lasers (QCLs) are unique solid state lasers that operate in the mid-infrared (IR) frequency range [1–4], which have such good features as wide tunability, compact device structure, and low power consumption. Among their various applications, gas sensing is especially promising, since the absorption lines of important gas molecules are covered by the QCL [5,6]. On the other hand, the conventional QCL is edge emission type, so their beam divergence is generally large, which may be an obstacle against their application to the remote sensing of dangerous gases and the extremely high-sensitivity gas analysis by a multiple laser-path configurations, for which high-quality laser beams with small divergence angles are needed because a long propagation length is required.

The surface-emission device configuration, known as VCSEL (vertical-cavity surface-emission laser), improves this problem of the laser-beam quality [7–10]. However, the VCSEL configuration is not applicable to QCL because of the mismatch between the polarization of emitted photons and that of the resonance cavity mode, since the QCL utilizes the inter-subband transitions of multiple quantum wells (MQWs) and they are transverse magnetically (TM) polarized [11,12]. On the other hand, the PCSEL (photonic-crystal surface-emitting laser) configuration with photonic crystal (PC) resonators [13–18] is also applicable to the surface-emitting QCL, since the cavity modes of the TM polarization can equally be materialized with the PC resonators [19–30].

In our previous study [29,30], we reported on surface-emitting PC-QCLs operating at 4.3 μm consisting of a strain-compensated MQW and a PC resonator. The maximum output power was still small and was 50 mw by a pulsed operation at 77 K with a 500 ns-wide

pulsed input current. The beam quality was rather good and an M^2 value of 1.4 was achieved. We adopted the square arrays of circular or pentagonal InGaAs pillars buried with InP for the PC resonator because those structures possessed a high spatial symmetry so that their characterization by reflection and emission measurements could efficiently be performed. Recently, we obtained 1.1 W peak power by reducing the symmetry of the PC unit cell.

In this paper, we report on these developments of surface-emitting mid-infrared QCLs jointly conducted by the National Institute for Materials Science, Toshiba Corporation, and Tokyo University of Technology, focusing on the relationship between the PC resonator structure and laser performance. We describe the design and characteristics of the PC resonator and show how they have improved the performance of the PC-QCL. Specifically, we present both numerical calculations by the finite element method (FEM) and analytical calculations by the $\mathbf{k} \cdot \mathbf{p}$ perturbation theory and group theory. We will discuss the resonance quality (Q) factor, overlap factor, extraction efficiency (EE), far-field pattern, and compare the main results with measured data of our PC-QCL devices.

2. Square-Lattice PC with Circular Pillars

We employed two-dimensional bulk PC resonators for our PC-QCL devices. On highly symmetric points like the Γ point of the Brillouin zone, the dispersion relation of the electromagnetic eigenmodes are often parabolic, so the group velocity is in the two-dimensional plane, which is given by

$$\mathbf{v}_g = \frac{\partial \omega}{\partial \mathbf{k}}, \tag{1}$$

where ω is the angular frequency and $\mathbf{k}$ is the two-dimensional wave vector, equal to zero. This means that such eigenmodes are standing waves and do not escape in the lateral directions. So, when their eigen frequencies coincide with the optical gain spectrum of the MQW consisting of the PC-QCL device, lasing takes place for input powers larger than the lasing threshold. For the Γ point ($\mathbf{k} = 0$), the lateral component of the wave vector of the emitted light must be equal to zero, so the emission takes place in the vertical direction. This is the main strategy for our surface-emitting QCL devices, which is the same as many of the PCSELs and surface-emitting QCLs ever reported. However, there are important details that are different from this simple explanation, which are brought about by the finite size of the actual PC resonator, the symmetry of the electromagnetic resonance mode, and the multi-mode lasing. We will describe these points in this paper.

For our first trial, we started with square-lattice PCs whose unit cells are illustrated in Figure 1a,b. We refer to such devices as PC-QCL-1 and PC-QCL-2, whereas those with the rectangular-lattice PCs are denoted by PC-QCL-3 (Figure 1c). Because the square lattice has a high symmetry, there are several selection rules in the light emission and reflection, which simplify the data analysis and facilitate the mode identification. Specifically, the unit cell of Figure 1a, which consists of a InGaAs circular pillar buried with InP, has the C_{4v} symmetry (the symmetry of square), so the eigenmodes on the Γ point are irreducible representations of the C_{4v} point group [31]. Note that the electric field is a genuine vector whereas the magnetic field is an axial vector, so their symmetries are generally different. We refer to the symmetry of the magnetic field in this paper. There are four one-dimensional representations (A_1, A_2, B_1, B_2) and one two-dimensional representation (E) on the Γ point, among which only the E mode, or the dipole mode, is active to the normal incident light and can radiate in the vertical direction if the PC structure is perfectly periodic and infinite. However, the actual PC has a finite size, which results in some interesting features of the emission angle and the FFP including their polarization dependence and anisotropy.

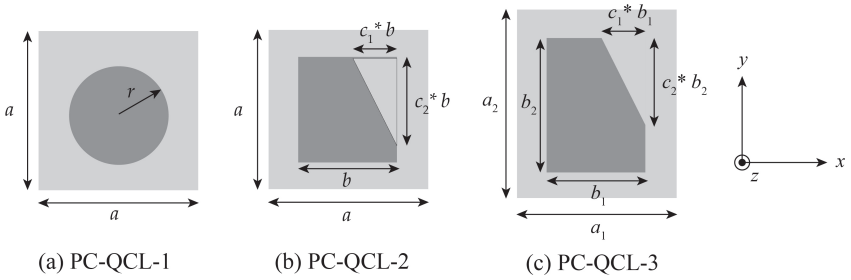

(a) PC-QCL-1 (b) PC-QCL-2 (c) PC-QCL-3

Figure 1. Top view of the unit cell composed of a InGaAs pillar (dark gray) buried with InP (light gray). (**a**) Square unit cell with a circular pillar. (**b**) Square unit cell with a pentagonal pillar. (**c**) Rectangular unit cell with a pentagonal pillar.

To examine the performance of the PC resonator, we first analyzed its electromagnetic eigenmodes assuming a perfectly periodic and infinite PC structure. For this purpose, we used commercial FEM software, COMSOL Multiphysics with the Wave Optics Module. We assumed the device structure shown in Figure 2a whose cross-sectional SEM image is presented in Figure 2b. We imposed a PML (perfectly matched layer) absorbing boundary conditions on the top and bottom ends of the computational volume and the Bloch boundary condition on the lateral surface of the unit cell to specify the wave vector **k**. For the details of materials and structural parameters assumed for this calculation, please refer to Ref. [29].

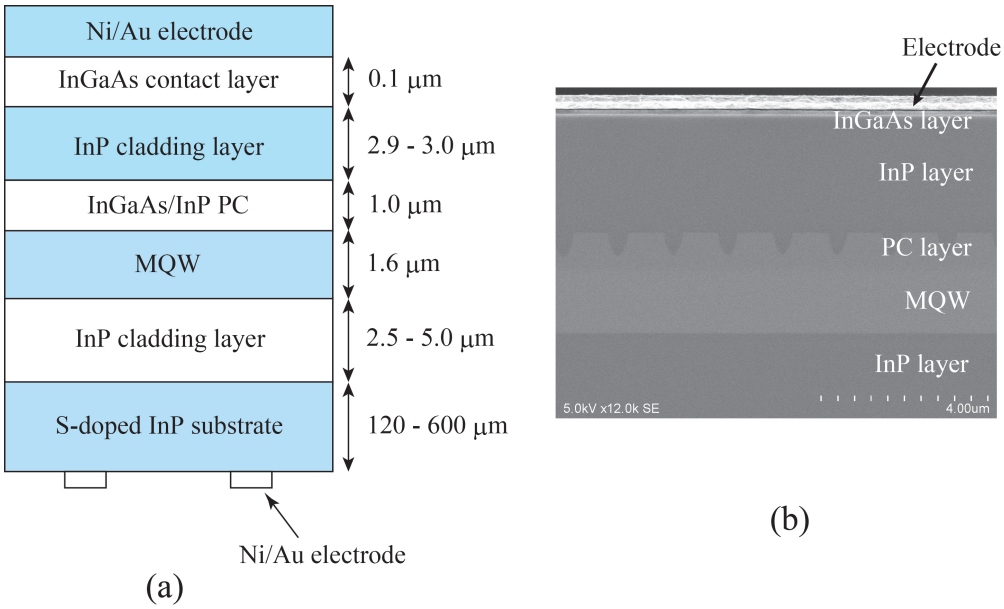

Figure 2. (**a**) Illustration of the side view of the device structure and (**b**) its cross–sectional SEM image.

Some results of the calculations for PC-QCL-1 are listed in the second row of Table 1. In the frequency range of our interest, which overlapped the optical gain spectrum of the MQW, there were four TM-like modes on the Γ point whose symmetries are shown in the second column. Among the five possible symmetries, we found E (doubly degenerate), A_2, and B_2 modes in this frequency range. Their resonance wavelengths were close to each other as a consequence of a small refractive-index contrast between the two components (InGaAs and InP) of the PC unit cell.

To illustrate this point, let us examine the empty-lattice dispersion curves; that is, the linear dispersion relation of a uniform material with a constant refractive index n folded back to the first Brillouin zone. Figure 3a is the empty-lattice dispersion with $n = 3.0$ for the square lattice, where "2" implies that the dispersion curve is doubly degenerate. The red circle shows the frequency range of the optical gain spectrum of the MQW of our

device. Because the $\pm x$ and $\pm y$ directions are all equivalent for the C_{4v} symmetric lattice, the number of modes degenerate on the Γ point is always a multiple of four except for $\omega = 0$ [32]. On the other hand, the x and y directions are not equivalent for the rectangular lattice, this number is reduced to two as shown in Figure 3b. This point is important to improve the extraction efficiency (EE) as we will see in Section 4.

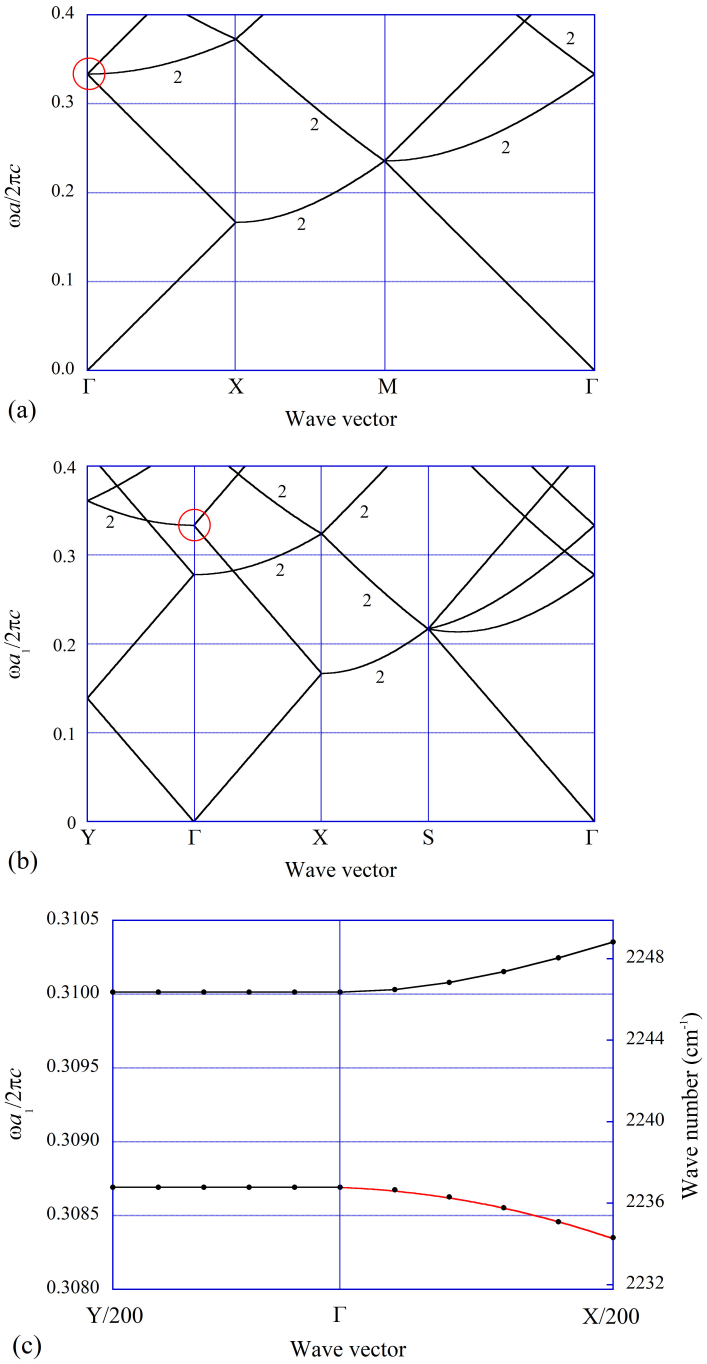

Figure 3. Dispersion curves of the purely two-dimensional empty-lattice PC with a uniform refractive index of 3.0 for (**a**) the square and (**b**) rectangular unit cells. The vertical axis on the left side is the dimensionless frequency, where ω is the angular frequency, c is the light velocity in free space, and a

and a_1 are the lattice constant of the square and rectangular PCs, respectively. The horizontal axis is the wave vector in the first Brillouin zone (see Figure 4). Red circles denote the frequency range of the eigenmodes on the Γ point that overlaps the optical gain spectrum of the MQW. The number "2" implies that the dispersion curve is doubly degenerate. (**c**) Magnified view of the dispersion curves of PC-QCL-3 calculated by FEM. The red line is the best fit by a parabolic function to the lower dispersion curve in the Γ-to-X direction. X/200 and Y/200 imply that the horizontal axis is magnified by 200 times.

Table 1. Comparison of typical eigenmode characters in the square and rectangular lattices. The designed sample parameters were as follows. $a = a_1 = 1.380$ μm, $a_2 = 1.2 \times a_1$, $b_1 = 0.900$ μm, $b_2 = 1.2 \times b_1$, $c_1 = 0.2$, $c_2 = 0.4$, height of InGaAs pillars = 0.8 μm.

Specimen	Mode	Wavelength (μm)	Q	Q_{abs}	Q_{dif}	Overlap Factor	EE (%)
PC-QCL-1	E	4.450	2778	2964	44,240	0.528	6.28
	A_2	4.441	3072	3072	∞	0.602	0 *
	B_2	4.432	3307	3307	∞	0.636	0 *
PC-QCL-2	TM1	4.464	2718	2870	51,190	0.524	5.31
	TM2	4.445	2904	3016	78,490	0.586	3.70
	TM3	4.442	2787	3078	29,520	0.600	9.44
	TM4	4.426	3445	3453	1.566×10^6	0.657	0.22
PC-QCL-3	TM1′	4.471	1910	2126	19,716	0.580	9.7
	TM2′	4.451	1337	2035	3976	0.631	33.6

* For A_2 and B_2 modes of PC-QCL-1, EE obtained by the band calculation is relevant to a perfectly periodic structure, for which the vertical emission is forbidden by symmetry, so EE is equal to zero. For the actual device, its lateral size was finite, so this selection rule was broken and a weak vertical emission was observed.

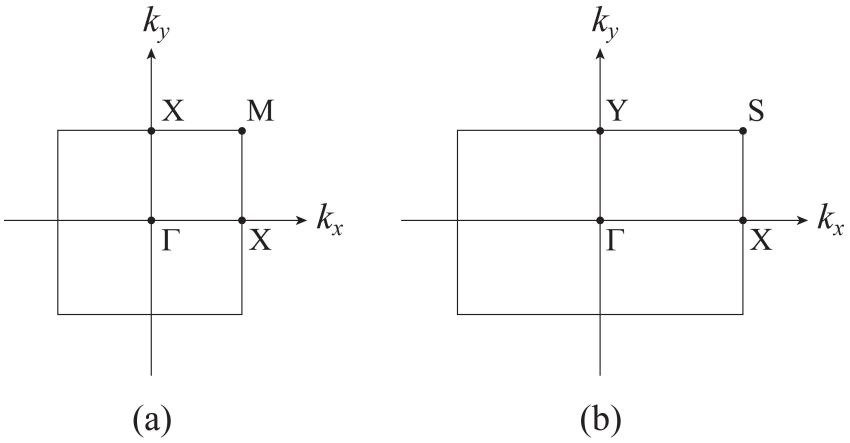

Figure 4. The first Brillouin zone of (**a**) the square lattice and (**b**) the rectangular lattice.

The characteristics of an optical resonator are listed in the third to seventh columns of Table 1. Q is the resonance quality factor, which is given by the ratio of the real part to the imaginary part of the eigen frequency ($\omega = \omega' + i\omega''$):

$$Q = \frac{\omega'}{2\omega''}. \tag{2}$$

On the other hand, Q_{abs} and Q_{dif} are the quality factors when the electromagnetic energy dissipation is only governed by the absorption or the diffraction in the vertical direction. Q^{-1} is given by their sum:

$$\frac{1}{Q} = \frac{1}{Q_{abs}} + \frac{1}{Q_{dif}}. \tag{3}$$

We calculated Q_{abs} by evaluating the Joule loss with the conductivity of the constituent materials and the electric-field distribution obtained by the eigenmode calculation (photonic-

band calculation) described above, whereas we obtained Q_{dif} by evaluating the electromagnetic energy flow to the vertical direction based on Poynting's vector. Their sum, as it should, agreed with Q. When we write down the same equation by using the decay rate, γ $(= \omega'/Q)$,

$$\gamma = \gamma_{\mathrm{abs}} + \gamma_{\mathrm{dif}}. \tag{4}$$

Then, EE is given by the ratio of the diffraction loss in the vertical direction to the total loss:

$$\mathrm{EE} = \frac{\gamma_{\mathrm{dif}}}{\gamma_{\mathrm{abs}} + \gamma_{\mathrm{dif}}} = \frac{Q_{\mathrm{abs}}}{Q_{\mathrm{abs}} + Q_{\mathrm{dif}}}. \tag{5}$$

So, a large absorption loss and/or a small diffraction loss results in a small EE. For the A_2 and B_2 modes of PC-QCL-1, the diffraction in the vertical direction is absent because of their symmetry mismatch with outside plane waves [32,33], so their EE is vanishing. This is also a consequence of the momentum conservation across the output aperture. This is true for the perfectly periodic infinite PC. However, the finite size of actual PCs partially breaks this momentum conservation law and enables the PC-QCL-1 to radiate in slightly oblique directions.

The overlap factor is defined by the ratio of the electric-field intensity distributed in the optically active MQW region to the total intensity, which estimates the coupling strength between electron and photon. Because the amount of the stimulated emission is proportional to the electric-field intensity, a large overlap factor is advantageous for lasing. Then, judging from the Q and overlap factors, we expected that the lasing threshold would be lowest for the B_2 mode. This expectation was confirmed by analyzing the polarization dependence of the FFP as we will describe below.

For this purpose and also for the evaluation of the escape rate in the lateral directions, γ_{lat}, and multi-mode lasing, we need to deal with small but non-zero $\mathbf{k}$. When we denote the lateral size of the PC by L, the wave vector, which is a continuous variable for the infinite lattice, is discretized as a multiple of π/L:

$$k = \frac{m\pi}{L} \qquad (m:\ \text{integer}). \tag{6}$$

So, we may roughly estimate that the wave vector has an ambiguity

$$\Delta k = \pm\frac{\pi}{2L}. \tag{7}$$

Then, the ambiguity in the emission angle is estimated at

$$\Delta\phi \approx \sin^{-1}\frac{\Delta k\lambda}{2\pi}, \tag{8}$$

where λ is the lasing wavelength. For our device, L was 500 μm and λ was about 4.3 μm, so $\Delta\phi$ was about $\pm 0.12^{\circ}$. This means that although the B_2 mode does not radiate in the vertical direction, it can radiate in slightly tilted directions for finite-size PCs. The dispersion curves are nearly isotropic around the Γ point, so as a result, the FFP is also isotropic and becomes a doughnut shape. This feature has been found in PCSELs and was actually observed in our PC-QCL-1 devices, too (See Figure 5a). For the measurements of FFP, we used a lensless mid-IR camera (IRV-T0831, NEC Corporation, Japan) located 26.8 mm away from the output aperture of the PC-QCL. The emission peak angle was about 0.25°, which was close to the above estimation.

This feature was brought about by the fact that the B_2 mode is inactive to the normal incident light. However, the A_2 mode has the same property, so we cannot judge which mode has lased from this feature alone. For this purpose, we can use the polarization dependence of the FFP. To derive it, we need to examine the relation between the electric-field polarization and the propagation direction for small k, which we can perform easily by using the vector-field version of the $\mathbf{k}\cdot\mathbf{p}$ perturbation theory [34].

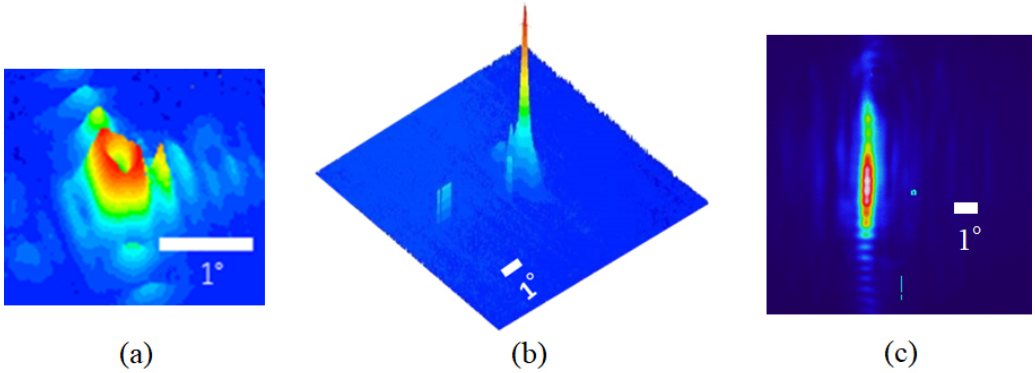

Figure 5. FFP of (**a**) PC-QCL-1, (**b**) PC-QCL-2, and (**c**) PC-QCL-3 measured with a mid-IR camera at 77 K. Panels (**a**,**b**) were obtained in the single-mode lasing condition whereas a multi-mode lasing took place for panel (**c**) (See text). The red and blue colors denote high-intensity and low-intensity regions of the FFP, respectively.

According to the Bloch theorem, the magnetic-field eigen function $\mathbf{H}_{\mathbf{k}l}$ is a product of a periodic vector field, $\mathbf{v}_{\mathbf{k}l}$, and an exponential factor:

$$\mathbf{H}_{\mathbf{k}l}(\mathbf{r}) = \mathbf{v}_{\mathbf{k}l}(\mathbf{r})e^{i\mathbf{k}\cdot\mathbf{r}}, \tag{9}$$

where l is the band index. For simplicity, we regard our PC-QCL configuration as a Hermitian system by imposing periodic boundary conditions on a large volume V and assuming the constituent materials are lossless. Then, the eigen frequencies of the electromagnetic eigen problems are real and their eigen functions are complete, so $\{\mathbf{v}_{\mathbf{k}l}|l = 1, 2, \dots\}$ for each $\mathbf{k}$ is an orthogonal complete set.

Then, we express $\mathbf{v}_{\mathbf{k}l}$ for non-zero but small $\mathbf{k}$ by a linear combination of $\mathbf{v}_{0j}$ with $\mathbf{k} = 0$ on the Γ point. Because we know the symmetry of $\mathbf{v}_{0j}$ very well, which must be A_1, A_2, B_1, B_2, or E, we can derive the main properties of $\mathbf{v}_{\mathbf{k}l}$ easily. As we mentioned earlier, there are only A_2, B_2, and E modes in the range of the MQW gain spectrum, and their eigen frequencies are close to each other. So, for the first-order approximation, we can ignore other modes. In addition, we showed in our previous study [34] that A_2 and B_2 modes do not mix with each other in the first-order perturbation. Then, we can approximate

$$\mathbf{v}_{\mathbf{k}}(\mathbf{r}) \approx f_1\mathbf{v}_E^{(1)}(\mathbf{r}) + f_2\mathbf{v}_E^{(2)}(\mathbf{r}) + f_3\mathbf{v}_\alpha(\mathbf{r}), \tag{10}$$

where $\mathbf{v}_E^{(1)}$ and $\mathbf{v}_E^{(2)}$ are two eigen functions of the doubly degenerate E mode, and α stands for A_2 or B_2. We can assume without loss of generality that $\mathbf{v}_E^{(1)}$ and $\mathbf{v}_E^{(2)}$ are transformed like x and y coordinates, respectively, by symmetry operations of the C_{4v} point group [31].

From Maxwell's wave equation, we can derive the eigen equation for $\mathbf{v}_{\mathbf{k}}$, which can be transformed to an eigen problem of a 3×3 matrix, $C_{\mathbf{k}}$, whose structure can be determined by the spatial symmetry of the basis functions. For the A_2 and B_2 modes, $C_{\mathbf{k}}$ has the following structures:

$$C_{\mathbf{k}} = \begin{pmatrix} 0, & 0, & bk_y \\ 0, & 0, & -bk_x \\ b^*k_y, & -b^*k_x, & \Delta \end{pmatrix} \quad \text{for } A_2, \tag{11}$$

$$C_{\mathbf{k}} = \begin{pmatrix} 0, & 0, & bk_y \\ 0, & 0, & bk_x \\ b^*k_y, & b^*k_x, & \Delta \end{pmatrix} \quad \text{for } B_2. \tag{12}$$

where b is a parameter determined by the structure of the PC and Δ describes the frequency difference between the two basis functions. Matrix $C_{\mathbf{k}}$ was originally derived for the

analysis of the Dirac-cone dispersion relation materialized by the accidental degeneracy of the two modes [34], so $\Delta = 0$ in that case. In the present case, it is given by

$$\Delta = \frac{\omega_\alpha^2 - \omega_E^2}{c^2}, \tag{13}$$

and the eigen equation is given by

$$C_{\mathbf{k}} \begin{pmatrix} f_1 \\ f_2 \\ f_3 \end{pmatrix} = \frac{\omega_{\mathbf{k}}^2 - \omega_E^2}{c^2} \begin{pmatrix} f_1 \\ f_2 \\ f_3 \end{pmatrix}. \tag{14}$$

By solving the secular equation, we obtain the eigenvalue in the first-order approximation:

$$\omega_{\mathbf{k}}^2 \approx \omega_\alpha^2 + \frac{|b|^2 c^2 k^2}{\omega_\alpha^2 - \omega_E^2}. \tag{15}$$

From Equation (14), we obtain f_1 and f_2:

$$f_1 = \frac{bk_y}{\omega_{\mathbf{k}}^2 - \omega_E^2} f_3, \qquad f_2 = \mp \frac{bk_x}{\omega_{\mathbf{k}}^2 - \omega_E^2} f_3, \tag{16}$$

while f_3 is determined by the normalization condition.

$$|f_1|^2 + |f_2|^2 + |f_3|^2 = 1. \tag{17}$$

In the expression of f_2 in Equation (16), the upper (lower) sign of $\mp$ applies to the A_2 (B_2) mode.

Next, we examine the connection of this local field around the PC to a far-field plane wave, $\mathbf{H}_{\mathbf{k}}^{(F)}$:

$$\mathbf{H}_{\mathbf{k}}^{(F)}(\mathbf{r}) = \mathbf{h}_0 e^{i\mathbf{k}'\cdot\mathbf{r}}, \tag{18}$$

where the wave vector of the emitted plane wave, $\mathbf{k}'$, is determined by the conservation of its lateral components:

$$k_x' = k_x, \qquad k_y' = k_y, \qquad c^2|\mathbf{k}'|^2 = \omega_{\mathbf{k}}^2. \tag{19}$$

On the other hand, by using the retarded Green's function, we can show that the connection coefficient $\xi_{\mathbf{k}}$ between $\mathbf{H}_k$ and $\mathbf{H}^{(F)}$ is simply given by the spatial average of their inner product [35]:

$$\xi_{\mathbf{k}} = \frac{1}{V} \int_V d\mathbf{r}\, \mathbf{H}_{\mathbf{k}}^*(\mathbf{r}) \cdot \mathbf{H}_{\mathbf{k}}^{(F)}(\mathbf{r}), \tag{20}$$

where V is a large volume on which periodic boundary conditions are imposed. We denote the wave vector $\mathbf{k}$ in the polar coordinates as

$$k_x = k\cos\phi, \qquad k_y = k\sin\phi, \tag{21}$$

whereas we denote the direction of the polarizer (electric field) by θ', which we assume is placed in front of the imaging plate to detect the FFP of PC-QCL-1. Then the direction of the magnetic field, $\mathbf{h}_0$, is $\theta = \theta' + 90^\circ$. By substituting Equations (10) and (18) into Equation (20), we finally obtain

$$|\xi_{\mathbf{k}}|^2 = \frac{|b|^2 h_0^2 k^2}{|b|^2 k^2 + \left(\omega_{\mathbf{k}}^2 - \omega_E^2\right)^2} \left| \overline{e^{ik_z' z} v_{\mathrm{E},x}^{(1)*}(\mathrm{r})} \right|^2 \cos^2(\phi \mp \theta'), \tag{22}$$

where the overline implies a spatial average. To derive Equation (22), we used the following symmetry properties of the basis functions.

$$v_{\alpha,x}(x,-y,z) = -v_{\alpha,x}(x,y,z), \tag{23}$$
$$v_{\alpha,y}(-x,y,z) = -v_{\alpha,x}(x,y,z), \tag{24}$$
$$v_{\mathrm{E},y}^{(1)}(-x,y,z) = -v_{\mathrm{E},y}^{(1)}(x,y,z), \tag{25}$$
$$v_{\mathrm{E},x}^{(2)}(-x,y,z) = -v_{\mathrm{E},x}^{(2)}(x,y,z), \tag{26}$$
$$v_{\mathrm{E},y}^{(2)}(x,y,z) = v_{\mathrm{E},x}^{(1)}(y,-x,z). \tag{27}$$

Because the $\cos^2$ function has two maxima between 0° and 360°, the FFP of the doughnut shape splits into two spots and they rotate in the same direction as the polarizer for the A_2 mode and in the opposite direction for the B_2 mode. The measurement of the polarization dependence showed that the two spots rotated in the opposite direction, so we confirmed that the lasing took place with the B_2 mode as we expected from the Q and overlap factors [30].

Although EE is not vanishing even for the A_2 and B_2 modes for finite-size PCs as we described so far, it is not as large as the E mode. So, lasing with the E mode is desirable to obtain a large output power. However, the Q and overlap factors are larger for the A_2 and B_2 modes, and so their lasing threshold is lower. Therefore, single-mode lasing with the E mode is difficult to achieve.

3. Square-Lattice PC with Pentagonal Pillars

To resolve this problem, we lowered the symmetry of the unit cell. Specifically, we examined PC-QCL-2 with a pentagonal InGaAs pillar buried with InP (See Figure 1b). As long as both of the two shape factors, c_1 and c_2, are not equal to zero, the symmetry of the unit cell is sufficiently low so that all modes on the Γ point can radiate in the vertical direction. In Table 1, some resonance-cavity properties calculated for $c_1 = 0.2$ and $c_2 = 0.4$ are listed. Because the eigenmodes of PC-QCL-2 do not possess any spatial symmetry, they are just numbered as TM1-TM4. The Q and overlap factors are largest for the TM4 mode, so we can expect that it will lase. For this case, EE is not large and is 0.22 %. This is because the refractive-index contrast is small and the field distribution and other properties of the TM4 mode are not so different from the B_2 mode of PC-QCL-1 even though the pillar shape was modified.

However, we achieved a larger output power with PC-QCL-2 as shown in Figure 6. We measured the peak output power with a pulsed input current. The pulse width was 500 ns and the repetition rate was 20 kHz. Specimens were attached to a cold finger of a liquid N_2 cryostat. The output was measured with a thermal power meter (Ophir, model 3A thermal sensor) located just in front of the cryostat. The thermal power meter was located as close to the device as possible so that all laser beams were detected by the photosensitive area of 9.5 mmϕ. The maximum peak power was 10 mW for PC-QCL-1 and 50 mW for PC-QCL-2. Although the output power was improved, the small EE was still a problem.

On the other hand, FFP was single peaked for PC-QCL-2 as shown in Figure 5b, which is distinct from the doughnut shape of PC-QCL-1. The M^2 value that characterizes the laser beam quality was as good as 1.4, which is another consequence of the symmetry reduction.

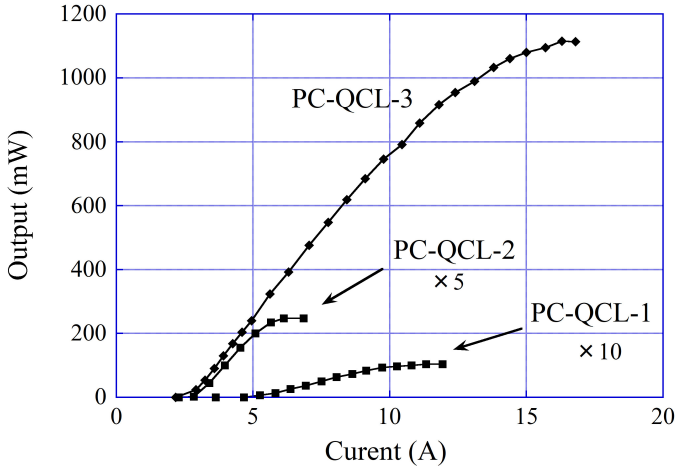

Figure 6. Peak output power of our PC-QCLs measured at 77 K with 500 ns pulsed input currents at a repetition rate of 20 kHz.

4. Rectangular-Lattice PC

To further improve the EE, we switched from the square lattice to the rectangular lattice. Then, we can decrease the number of eigenmodes that are located in the gain spectrum of the MQW. Specifically, we can divide the four eigenmodes on the Γ point into two groups as shown in Figure 3b to locate only one of the two group in the gain spectrum. By this method, we can exclude such eigenmodes whose Q_{dif} is unnecessarily high. As a matter of fact, the fourth row of Table 1 shows the resonance-cavity properties of the two TM-like modes on the Γ point that were located in the gain spectrum. Their Q factors and EE are moderate values. As shown in Figure 6, we achieved a peak output power of 1.1 W, which was considerably larger than PC-QCL-1 and PC-QCL-2 with square-lattice PCs. For PC-QCL-3, the InP substrate was thinned down to 120 μm from its original value of 600 μm, so the reduction in the absorption by the substrate also contributed to the increase in the output power.

On the other hand, the anisotropy of the PC unit cell in PC-QCL-3 results in the anisotropy of the FFP when the input power is sufficiently larger than the lasing threshold and the multi-mode lasing takes place. To describe this feature, let us examine the dispersion curves more closely. Due to the rectangular shape of the unit cell, the x and y directions are not equivalent to each other. This results in the big anisotropy of the dispersion curves. A magnified view of the dispersion curves of PC-QCL-3, which were obtained by photonic-band calculation by FEM, are presented in Figure 3c, where those two modes whose eigen frequencies are located in the MQW gain spectrum are plotted. It is clear that the dispersion is highly anisotropic, and it is nearly flat in the Γ-to-Y direction, which is anticipated from the empty-lattice dispersion in Figure 3b. For PC-QCL-2, the unit–cell structure is also anisotropic due to the pentagonal shape of the InGaAs pilar. However, the anisotropy of the dispersion curves is relatively small because of the small refractive-index contrast between InGaAs and InP.

The key point that governs the anisotropy of the FFP is the escape rate of the electromagnetic energy in the lateral directions. We previously mentioned that the total decay rate (γ) of the resonance-cavity mode is given by the sum of the absorption rate (γ_{abs}) and the diffraction rate (γ_{dif}) for perfectly periodic infinite PCs. However, for PCs with a finite size, the energy dissipation in the lateral directions (γ_{lat}) cannot be ignored. Thus, we have

$$\gamma = \gamma_{\mathrm{abs}} + \gamma_{\mathrm{dif}} + \gamma_{\mathrm{lat}}. \tag{28}$$

If γ_{lat} is small for certain eigenmodes, it does not lower the Q factor. So, those modes with small γ_{lat} are candidates for multi-mode lasing when the input power is sufficiently large.

The accurate numerical evaluation of γ_{lat} is not easy because we have to deal with a large sample volume compared with the wavelength of the relevant electromagnetic eigenmode. However, there is a rough but simple estimation of γ_{lat} obtained from the dispersion relation of the infinite PC. In the case of lossless PCs, we can show by an exact analytical calculation that the energy velocity of the electromagnetic eigenmode is equal to its group velocity [32,36]. Here, we assume that it also holds approximately in our case. The escape time in the lateral direction is given by the average distance for the escape, $L/2$, divided by the group velocity. Then, the escape rate, γ_{lat}, is its inverse:

$$\gamma_{\mathrm{lat}} = \frac{2v_{\mathrm{g}}(k)}{L}. \tag{29}$$

As an example, let us estimate γ_{lat} for the lower branch in the Γ-to-X direction in Figure 3c. The red line in this figure is the best fit to the calculated eigen frequencies by a parabolic function. From the coefficients obtained by the curve fitting, we could calculate the first derivative of ω with respect to k. Thus, we obtained

$$\gamma_{\mathrm{lat}} = 45.3 \times \frac{a_1 c k_x}{2\pi L}, \tag{30}$$

where a_1 is the lattice constant in the x direction (See Figure 1c). For the first Fabry–Perot mode with $k_x = \pm\pi/L$, for example, Q_{lat} was obtained as follows:

$$Q_{\mathrm{lat}} = \frac{\omega'}{\gamma_{\mathrm{lat}}} = 2780, \tag{31}$$

which reduces the total Q factor of 1910 on the Γ point to 1130. This value is smaller than the TM2′ mode (See Table 1), so we may safely ignore the possibility of the lasing by the first-order Fabry–Perot mode compared with the TM2′ mode. On the other hand, the two dispersion curves are much flatter in the Γ-to-Y direction, so v_{g} is much smaller, and Q_{lat} is larger. The same estimation leads to $Q_{\mathrm{lat}} = 10^6$ for the first Fabry–Perot mode. This means that those eigenmodes with small k_y have total Q factors that are very close to that of the Γ point, so their lasing thresholds are similar to each other. As a result, multi-mode lasing easily takes place in the y direction and its FFP becomes elongated in the y direction, which was actually observed with PC-QCL-3 as shown in Figure 5c.

5. Conclusions

We described our recent development of surface-emitting quantum cascade lasers mainly from the viewpoint of the design of the PC resonators. We showed that we could control the coupling between the resonance mode and the outside electromagnetic field both qualitatively and quantitatively by changing the symmetry of the PC unit cell. Specifically, we developed a $\mathbf{k} \cdot \mathbf{p}$ perturbation theory to analyze the polarization dependence of the FFP, which enabled us to identify the resonance mode responsible for lasing in the case of highly symmetric unit cells. On the other hand, by reducing the symmetry and employing the rectangular unit cell, we could efficiently control the diffraction Q factor to obtain a moderate EE even with a small refractive-index contrast between the constituent materials of the PC unit cell. Thus, we achieved a 1.1 W peak output power at 4.3 μm with a 500 ns input-current pulse width at 77 K by fabricating PC-QCLs with a strain-compensated MQW active layer.

Funding: This work was supported by the Innovative Science and Technology Initiative for Security, Grant No. JPJ004596, ATLA, Japan

Conflicts of Interest: Authors Rei Hashimoto, Kei Kaneko, Tsutomu Kakuno, Shinji Ohkuma, Ryuichi Togawa, Tetsuya Miyagawa, Hiroshi Ohno, and Shinji Saito are employed by Toshiba Corporation's Corporate Manufacturing Engineering Center. The remaining authors declare that the

research was conducted without any commercial or financial relationships that could be viewed as a potential conflict of interest.

Abbreviations

The following abbreviations are used in this manuscript:

EE	Extraction efficiency
FFP	Far field pattern
MQW	Multiple quantum well
PC	Photonic crystal
PCSEL	Photonic-crystal surface-emitting laser
Q	Quality
QCL	Quantum cascade laser
TM	Transverse magnetical
VCSEL	Vertical-cavity surface-emission laser

References

1. Faist, J.; Capasso, F.; Sivco, D.L.; Sirtori, C.; Hutchinson, A.L.; Cho, A.Y. Quantum cascade laser. *Science* **1994**, *264*, 553. [CrossRef] [PubMed]
2. Beck, M.; Hofstetter, D.; Aellen, T.; Faist, J.; Oesterle, U.; Ilgems, M.; Gini, E.; Melchior, H. Continuous wave operation of a mid-infrared semiconductor laser at room temperature. *Science* **2002**, *295*, 301. [CrossRef] [PubMed]
3. Slivken, S.; Evans, A.; David, J.; Razeghi, M. High-average-power, high-duty-cycle ($\lambda \sim 6$ μm) quantum cascade lasers. *Appl. Phys. Lett.* **2002**, *81*, 4321. [CrossRef]
4. Evans, A.; Yu, J.S.; Slivken, S.; Razeghi, M. Continuous-wave operation of $\lambda \sim 4.8$ μm quantum-cascade lasers at room temperature. *Appl. Phys. Lett.* **2004**, *85*, 2166. [CrossRef]
5. Tittel, F.K.; Bakhirkin, Y.; Kosterev, A.A.; Wysocki, G. Recent advances in trace gas detection using quantum and interband cascade lasers. *Rev. Laser Eng.* **2006**, *34*, 275. [CrossRef]
6. Maekawa, A.; Shiomi, Y.; Uchida, M.; Kakuno, T. QCL-based trace gas analyzer for industrial and healthcare applications. *Proc. SPIE* **2017**, *10111*, 1011106.
7. Iga, K.; Koyama, F.; Kinoshita, S. Surface emitting semiconductor lasers. *IEEE J. Quantum Electron.* **1988**, *24*, 1845. [CrossRef]
8. Iga, K. Surface-emitting laser-its birth and generation of new optoelectronics field. *IEEE J. Sel. Top. Quantum Electron.* **2000**, *6*, 1201. [CrossRef]
9. Takaoka, K.; Ishikawa, M.; Hatakoshi, G. Low-threshold and high-temperature operation of InGaAlP-based proton-implanted red VCSELs. *IEEE J. Sel. Top. Quantum Electron.* **2001**,*7*, 381. [CrossRef]
10. Iga, K. Forty years of vertical-cavity surface-emitting laser: Invention and innovation. *Jpn. J. Appl. Phys.* **2018**, *57*, 08PA01 . [CrossRef]
11. Sirtori, C.; Capasso, F.; Faist, J.; Sivco, D.L.; Hutchinson, A.L.; Cho, A.Y. Quantum cascade unipolar intersubband light emitting diodes in the 8–13 μm wavelength region. *Appl. Phys. Lett.* **1995**, *66*, 4. [CrossRef]
12. Faist, J. *Quantum Cascade Lasers*; Oxford University Press: Oxford, UK, 2013.
13. Imada, M.; Noda, S.; Chutinan, A.; Tokuda, T.; Murata, M.; Sasaki, G. Coherent two-dimensional lasing action in surface-emitting laser with triangular-lattice photonic crystal structure. *Appl. Phys. Lett.* **1999**, *75*, 316. [CrossRef]
14. Noda, S.; Yokoyama, M.; Imada, M.; Chutinan, A.; Mochizuki, M. Polarization mode control of two-dimensional photonic crystal laser by unit cell structure design. *Science* **2001**, *293*, 1123 . [CrossRef] [PubMed]
15. Williams, D.M.; Groom, K.M.; Stevens, B.J.; Childs, D.T.D.; Taylor, R.J.E.; Khamas, S.; Hogg, R.A.; Ikeda, N.; Sugimoto, Y. Optimisation of coupling between photonic crystal and active elements in an epitaxially regrown GaAs based photonic crystal surface emitting laser. *Jpn. J. Appl. Phys.* **2012**, *51*, 02BG05. [CrossRef]
16. Hirose, K.; Liang, Y.; Kurosaka, Y.; Watanabe, A.; Sugiyama, T.; Noda, S. Watt-class high-power, high-beam-quality photonic-crystal lasers. *Nat. Photonics* **2014**, *8*, 406. [CrossRef]
17. Noda, S.; Kitamura, K.; Okino, T.; Yasuda, D.; Tanaka, Y. Photonic-crystal surface-emitting lasers: Review and introduction of modulated-photonic crystals. *IEEE J. Sel. Top. Quantum Electron.* **2017**, *23*, 4900107. [CrossRef]
18. Morita, R.; Inoue, T.; Zoysa, M.D.; Ishizaki, K.; Noda, S. Photonic-crystal lasers with two-dimensionally arranged gain and loss sections for high-peak-power short-pulse operation. *Nat. Photonics* **2021**, *15*, 311. [CrossRef]
19. Colombelli, R.; Srinivasan, K.; Troccoli, M.; Painter, O.; Gmachl, C.F.; Tennant, D.M.; Sergent, A.M.; Sivco, D.L.; Cho, A.Y.; Capasso, F. Quantum cascade surface-emitting photonic crystal laser. *Science* **2003**, *302*, 1374. [CrossRef]
20. Bai, Y.; Gökden, B.; Darvish, S.R.; Slivken, S.; Razeghi, M. Photonic crystal distributed feedback quantum cascade lasers with 12 W output power. *Appl. Phys. Lett.* **2009**, *95*, 031105. [CrossRef]
21. Gökden, B.; Bai, Y.; Bandyopadhyay, N.; Slivken, S.; Razeghi, M. Broad area photonic crystal distributed feedback quantum cascade lasers emitting 34 W at $\lambda \sim 4.36$ μm. *Appl. Phys. Lett.* **2010**, *97*, 131112. [CrossRef]

22. Wu, D.H.; Razeghi, M. High power, low divergent, substrate emitting quantum cascade ring laser in continuous wave operation. *APL Mater.* **2017**, *5*, 035505. [CrossRef]
23. Mahler, L.; Tredicucci, A. Photonic engineering of surface-emitting terahertz quantum cascade lasers. *Laser Photon. Rev.* **2011**, *5*, 647. [CrossRef]
24. Diao, Z.; Bonzon, C.; Scalari, G.; Beck, M.; Faist, J.; Houdre, R. Continuous-wave vertically emitting photonic crystal terahertz laser. *Laser Photon. Rev.* **2013**, *7*, L45. [CrossRef]
25. Liang, Y.; Wang, Z.; Wolf, J.; Gini, E.; Beck, M.; Meng, B.; Faist, J.; Scalari, G. Room temperature surface emission on large-area photonic crystal quantum cascade lasers. *Appl. Phys. Lett.* **2019**, *114*, 031102. [CrossRef]
26. Wang, Z.; Liang, Y.; Meng, B.; Sun, Y.-T.; Omanakuttan, G.; Gini, E.; Beck, M.; Sergachev, I.; Lourdudoss, S.; Faist, J.; et al. Large area photonic crystal quantum cascade laser with 5 W surface-emitting power. *Opt. Express* **2019**, *27*, 22708. [CrossRef]
27. Stark, D.; Kapsalidis, F.; Markmann, S.; Bertrand, M.; Marzban, B.; Gini, E.; Beck, M.; Faist, J. Quantum cascade surface emitting lasers. *Laser Photon. Rev.* **2024**, *18* 2300663. [CrossRef]
28. Yao, D.-Y.; Zhang, J.-C.; Cathabard, O.; Zhai, S.-Q.; Liu, Y.-H.; Jia, Z.-W.; Liu, F.-Q.; Wang, Z.-G. 10-W pulsed operation of substrate emitting photonic-crystal quantum cascade laser with very small divergence. *Nanoscale Res. Lett.* **2015**, *10*, 177. [CrossRef]
29. Saito, S.; Hashimoto, R.; Kaneko, K.; Kakuno, T.; Yao, Y.; Ikeda, N.; Sugimoto, Y.; Mano, T.; Kuroda, T.; Tanimura, H.; et al. Design and fabrication of photonic crystal resonators for single-mode and vertical surface emission from strain-compensated quantum cascade lasers operating at 4.32 μm. *Appl. Phys. Express* **2021**, *14*, 102003. [CrossRef]
30. Yao, Y.; Ikeda, N.; Chalimah, S.; Kuroda, T.; Sugimoto, Y.; Mano, T.; Koyama, H.; Hashimoto, R.; Kaneko, K.; Kakuno, T.; et al. Improved power and far-field pattern of surface-emitting quantum cascade lasers with strain compensation to operate at 4.3 μm. *Jpn. J. Appl. Phys.* **2022**, *61*, 052001. [CrossRef]
31. Inui, T.; Tanabe, Y.; Onodera, Y. *Group Theory and Its Applications in Physics*; Springer: Berlin, Germany, 1990.
32. Sakoda, K. *Optical Properties of Photonic Crystals*, 2nd ed.; Springer: Berlin, Germany, 2004.
33. Ochiai, T.; Sakoda, K. Dispersion relation and optical transmittance of a hexagonal photonic crystal slab. *Phys. Rev. B* **2001**, *63*, 125107. [CrossRef]
34. Sakoda, K. Proof of the universality of mode symmetries in creating photonic Dirac cones. *Opt. Express* **2012**, *20*, 25181. [CrossRef] [PubMed]
35. Sakoda, K. Polarization-dependent continuous change in the propagation direction of Dirac-cone modes in photonic crystal slabs. *Phys. Rev. A* **2014**, *90*, 013835. [CrossRef]
36. Yeh, P. Electromagnetic propagation in birefringent layered media. *J. Opt. Soc. Am.* **1979**, *69*, 742. [CrossRef]